J. Fluid Mech. (2009), *vol.* 623, *pp.* 1–26.
doi:10.1017/S0022112008003911 Printed in the United Kingdom

Fluid mechanics of the flow-excited Helmholtz resonator

RUOLONG MA†, PAUL E. SLABOCH AND SCOTT C. MORRIS

Hessert Laboratory for Aerospace Research, Department of Aerospace and Mechanical Engineering, University of Notre Dame, Notre Dame, IN 46556, USA

(Received 14 April 2008 and in revised form 27 August 2008)

A flow-excited Helmholtz resonator was investigated experimentally and theoretically. The analysis was focused on a simplified momentum balance integrated over the region of the orifice. The resulting expressions were used to guide an experimental programme designed to obtain measurements of the resonator pressure under flow excitation, as well as the dynamics of the shear layer in the orifice using particle image velocimetry (PIV). The pressure measurements indicated a number of distinctive features as the flow speed varied. The PIV results provided a detailed representation of the shear layer vorticity field, as well as the equivalent hydrodynamic forcing of the resonator. The forcing magnitude was found to be roughly constant over a range of flow speeds. A model was proposed that provides a prediction of the resonator pressure fluctuations based on the thickness of the approach boundary layer, the free stream speed and the acoustic properties of the resonator. The model was shown to provide an accurate representation of the resonating frequency as well as the magnitude of the resonance to within a few decibels.

1. Introduction

This paper presents a detailed study of a flow-excited Helmholtz resonator. An example of this phenomenon is the resonance that occurs when blowing over the orifice of a glass bottle. The same physical process is present when an automobile is travelling with a single window lowered. This is often termed 'window buffeting' and results in an uncomfortable level of cabin pressure fluctuations.

A 'Helmholtz resonator' is a device in which a volume of compressible fluid is enclosed by rigid boundaries with a single, small opening (Kinsler *et al.* 2000). The resonator is easily modelled by a second-order mass-spring system analogy, where the fluid in the region of the orifice acts as the effective mass, and the compressibility of the fluid in the volume acts as a stiffness. Acoustic radiation and viscous effects both lead to an effective damping. The resonator natural frequency is given by $f_{hr} = (c/2\pi)\sqrt{S/\mathscr{V}l}$, where S is the area of the orifice; l is the effective neck thickness; $\mathscr{V}$ is the volume of the resonator; and c is the speed of sound. Near this frequency, a small pressure disturbance can produce a large-magnitude velocity fluctuation at the orifice and thus a large pressure fluctuation within the resonator. The acoustic wavelength that corresponds to the natural frequency is large compared to the dimensions of the resonator. Specifically, $\lambda \gg \sqrt[3]{\mathscr{V}}$, such that the unsteady pressure

† Email address for correspondence: r.ma@nd.edu

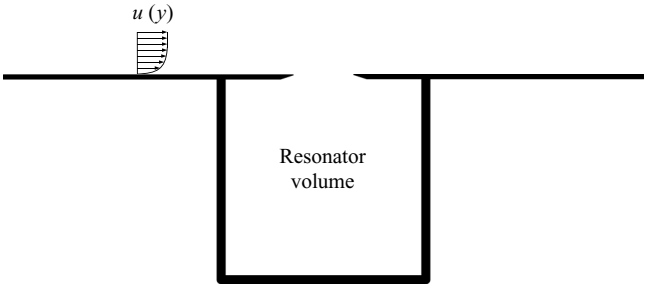

FIGURE 1. Schematic of a simplified Helmholtz resonator with knife-edge opening.

inside the volume can be considered to be spatially uniform. Similarly, $\lambda \gg L$, where L is the characteristic length of the orifice, and so the region outside of the enclosed volume can be modelled acoustically with the orifice acting as a compact baffled piston.

The flow-excited Helmholtz resonator geometry considered here is shown in figure 1. This configuration shows a grazing flow in which the wall boundary layer separates at the sharp edge and flows over the resonator orifice. The vorticity forms a shear layer that is unconstrained in the cross-stream direction over the the orifice length, L. This flow is well understood to be linearly unstable to disturbances at discrete values of the dimensionless frequency: fL/U (see e.g. Howe 1997; Chaterllier, Laumonier & Gervais 2004). Flow-excited resonance occurs when one of the hydrodynamic instability frequencies, or 'modes,' are close to the resonator natural frequency. The primary independent variable is typically the free stream velocity of the grazing flow, U. In other words, the pressure fluctuations in the resonator are the maximum at the specific velocity at which the time scale of the most unstable shear-layer mode is equal to the time scale of the resonator volume. In most applications, notably the glass bottle and automobile window, the velocity at which the fluctuations are the maximum will be at a relatively low Mach number, say $Ma < 0.1$.

It is important to note the similarities and differences between the flow-excited Helmholtz resonator and a number of similar configurations. Foremost is the classic problem of high Mach number flow over a shallow cavity studied by Rossiter (1964). This geometry exhibits a shear layer disturbance that grows over the cavity opening and impinges on the cavity trailing edge. This interaction results in a large pressure fluctuation that travels upstream as an acoustic wave. The acoustic disturbance causes the next disturbance in the shear layer, which leads to self-sustained oscillations. The resonance, or 'Rossiter mode,' exists when the instability time scale of the shear layer is close to the acoustic travel time from one end of the cavity to the other. As a result, the acoustic wavelength and the orifice length scale are of the same order ($\lambda \approx L$). Note also that the feedback disturbances in the shallow cavity problem necessarily travel in a direction parallel to the plane of the shear layer. This is an important contrast to the present problem in which the resonator volume responds with a disturbance that is perpendicular to the shear layer.

There are a number of additional configurations that share some characteristics with the presently considered boundary conditions. For example, shallow cavities, deep cavities, branched pipe flow and gap flows all exhibit some type of flow-excited resonance. A thorough review was given by Rockwell & Naudascher (1978). More recent work involving shallow cavities includes that of Graf & Durgin (1993) and Chatellier *et al.* (2004). Note, however, that the flow-excited Helmholtz resonator is considered to be unique and distinct from similar configurations involving shallow

cavities and the like. A recent review of dynamics and control of shallow cavity flow is given by Rowley & Williams (2006).

Early work that was focused specifically on flow over a Helmholtz resonator described the basic features of the resonator pressure fluctuations with a variety of geometries and inflow conditions (Panton & Miller 1975; Elder, Frabee & DeMetz 1982). Nelson, Halliwell & Doak (1981) provided detailed measurements of both the resonator pressure and the flow field in the vicinity of the orifice. Flow visualization and velocity measurements were interpreted to indicate that the resonance is caused by the shedding of a single discrete vortex from the orifice edge, which travels over the opening during one cycle of the oscillation. Nelson *et al.* (1983) later developed a detailed analysis of the flow field based on both linear momentum and energy principles. They concluded that the unsteady velocity–vorticity cross-product was the primary variable linked to the self-sustained resonance. More recent work has focused on the experimental and numerical determinations of the resonator pressure fluctuations under a wide variety of boundary conditions. For example, the effects of the orifice geometry has been studied by Panton (1990), Dequand *et al.* (2003*a*, *b*), and Amandolèse *et al.* (2004).

Methods for predicting the resonator pressure have received significant attention. One method, originally proposed by Elder (1978) for a deep cavity geometry, is the framework of a feedback loop system analysis. The hydrodynamic forcing was considered a 'forward gain function,' and the resonator acoustics were considered a 'backward gain function.' The resonator pressure amplitude was then found by equating the amplitude and phase of the two gain functions. Mast & Pierce (1995) later applied a similar technique, termed 'describing-function theory,' in which the forward gain function was described analytically by the dipole-like interaction of the vorticity with the trailing edge of the orifice. Based on a dimensionless tuning parameter, termed β, the theory was able to accurately capture the resonator pressure amplitude as a function of free stream speed. Kook & Mongeau (2002) later developed a similar analysis but modelled the forward gain function on a point vortex model. They also found that a tuning parameter, termed α, that allows the theory to accurately predict the resonator pressures under a wide variety of flow conditions could be found.

The most recent literature on the subject of flow-excited Helmholtz resonators has included a number of large-scale numerical studies (Inagaki *et al.* 2002; Mallick, Shock & Yakhut 2003; Crouse *et al.* 2006). The agreement with experimental data varied and in some cases required arbitrary scaling of the data. For example Mallick *et al.* (2003) multiplied the free stream speed of Nelson *et al.* (1981) by a factor of 15/22 in order to demonstrate agreement with the predicted resonator pressure values. They attributed this to be a result of the effects of boundary layer thickness on the effective speed of the shear layer.

The objective of the present research is to provide a complete description of the fluid dynamic characteristics of a flow-excited Helmholtz resonator. The description of the problem will first be given in the context of a linear momentum balance. The resulting expressions will be shown to provide a simple relationship between the shear layer dynamics and the compression of the resonator fluid. Detailed measurements of the resonator pressure as well as particle image velocimetry (PIV) measurements in the region of the orifice will be described in the context of the terms derived in the momentum balance. Lastly, a predictive methodology will be described based on the results of the detailed measurements. The theory will be validated against measurements available in the open literature.

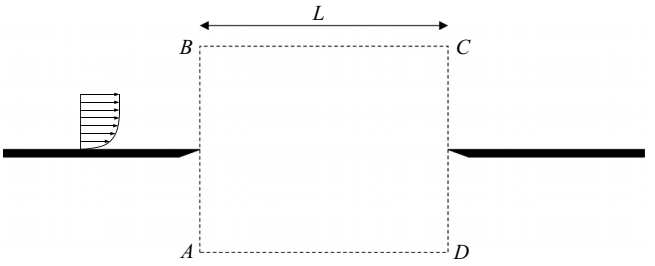

FIGURE 2. Schematic of the control volume for momentum analysis.

2. Theoretical analysis

Consider a resonator with a knife-edge rectangular window as shown in figure 2. The streamwise window length is L; the area of the window is S; and the resonator volume is $\mathscr{V}$. A useful starting point for the analysis is the Euler equation in Crocco's form given by

$$\frac{\partial \boldsymbol{V}}{\partial t} + \frac{1}{\rho}\nabla p = -\boldsymbol{\omega} \times \boldsymbol{V} - \nabla \frac{|\boldsymbol{V}|^2}{2}. \tag{2.1}$$

The control volume of interest is outlined in figure 2, with respective corners labelled $(ABCD)$. The flow is assumed to be uniform along the spanwise direction; so only a two-dimensional cross-section is drawn. The upper (BC) and lower (AD) sides of the volume are placed such that the flow can be considered irrotational at these boundaries. The vertical component of Crocco's equation can then be integrated over the area enclosed by the four sides (i.e. in the plane of figure 2) to yield

$$\int \rho \frac{\partial v}{\partial t} \mathrm{d}A + (p_{BC} - p_{AD})L = -\int \rho u \omega_z \, \mathrm{d}A - \frac{1}{2}\rho\left(|\boldsymbol{V}|^2_{BC} - |\boldsymbol{V}|^2_{AD}\right)L. \tag{2.2}$$

Here ω_z denotes the spanwise vorticity component, and u and v are respectively the streamwise and vertical velocity components. The pressure along (BC) and (AD) is assumed to be uniform.

The self-sustained resonance is periodic, and so it is instructive to consider the Fourier transform of (2.2):

$$\int \rho \left(\frac{\partial v}{\partial t}\right)^{\wedge} \mathrm{d}A + (\hat{p}_{BC} - \hat{p}_{AD})L = -\int \rho (u\omega_z)^{\wedge} \, \mathrm{d}A, \tag{2.3}$$

where the superscript $^{\wedge}$ denotes a Fourier transformed variable. Note the unsteady components of velocity along (BC) and (AD) are neglected, since both are considered to be far from the unsteady shear layer motions, and the acoustic velocity is also considered to be small. The unsteady pressure, $\hat{p}_{BC}$, is a result of incoming and outgoing acoustic waves. Incoming acoustic waves will result in the excitation of the resonator and are denoted as $\hat{p}_{exc}$. Outgoing waves are a result of acoustic radiation from the orifice and denoted as $\hat{p}_{rad}$. The unsteady pressure $\hat{p}_{AD}$ represents the pressure inside the resonator and is denoted as $\hat{p}_{res}$. Division of (2.3) by $\hat{p}_{res}L$ yields

$$\frac{\hat{p}_{exc} + \frac{1}{L}\int \rho (u\omega_z)^{\wedge} \, \mathrm{d}A}{\hat{p}_{res}} = \frac{1}{\hat{p}_{res}L}\left[-\int \rho \left(\frac{\partial v}{\partial t}\right)^{\wedge} \mathrm{d}A - \hat{p}_{rad}L + \hat{p}_{res}L\right] \equiv Z^*. \tag{2.4}$$

The left-hand side of (2.4) represents the ratio of the total external excitation to the resonator pressure. The two terms in the numerator on the left-hand side can

be interpreted as the external excitation of the resonator due to incoming acoustic waves and the 'hydrodynamic forcing' due to the unsteady vorticity in the shear layer, respectively.

The righthand side is the transfer function of the resonator system, denoted as Z^*, and can be shown to be equivalent to the non-dimensional mechanical impedance of the system. Specifically, the righthand side of (2.4) can be approximated by a lumped element model for an ideal Helmholtz resonator in the manner described: First, the area integral of the unsteady vertical component of velocity represents the unsteady inertia of the fluid inside the control surface (per unit width W). One can consider this in terms of a net or bulk inertia by defining $(M/W)\bar{v} \equiv \int \rho v \, \mathrm{d}A$. Here M is the equivalent mass of the control volume. The unsteady inertia can be represented by $-(M/W)(\mathrm{d}^2\xi/\mathrm{d}t^2)$, where ξ is the vertical effective displacement of the mass with the downward direction (pointing into the resonator) as positive.

The radiation pressure can be written in terms of the orifice fluid displacement as $p_{rad}L = -(R_r/W)\mathrm{d}\xi/\mathrm{d}t$ based on a Rayleigh integral, where R_r is an effective radiation resistance (see Crighton *et al.* 1992). The resonator pressure $\hat{p}_{res}$ can be related to the displacement of $\hat{\xi}$ by (Dowling & Ffowcs Williams 1983),

$$\hat{p}_{res}L = (K/W)\hat{\xi}, \tag{2.5}$$

where the stiffness K is defined as $(\rho_0 c^2 S^2)/\mathscr{V}$, and ρ_0 is the equilibrium density.

Substituting all of the above representations into Z^* leads to the lumped element model (LEM) representation

$$Z^*_{LEM} \equiv \frac{M\left(\dfrac{\mathrm{d}^2\xi}{\mathrm{d}t^2}\right)^{\wedge} + R\left(\dfrac{\mathrm{d}\xi}{\mathrm{d}t}\right)^{\wedge} + K\hat{\xi}}{K\hat{\xi}}; \tag{2.6}$$

R represents the summation of the radiation resistance (R_r) and a net viscous resistance arising from the losses due to the wall. The amplitude $\hat{\xi}$ can be removed from (2.6) to yield

$$Z^*_{LEM} = \frac{-4\pi^2 f^2 M + \mathrm{i}2\pi f R + K}{K} = -f^{*2} + \mathrm{i}f^*/Q + 1, \tag{2.7}$$

where f^* denotes the non-dimensional frequency f/f_{hr}. The resonator natural frequency $f_{hr} = \sqrt{K/M}/2\pi$, and the quality factor $Q = 2\pi f_{hr} M/R$. Z^*_{LEM} represents the non-dimensional mechanical impedance of a standard second-order system.

A simplified expression for the momentum balance is obtained for the conditions in which there is no grazing flow over the orifice. Specifically, when only acoustic excitation is present (2.4) reduces to

$$\frac{\hat{p}_{exc}}{\hat{p}_{res}} = Z^*. \tag{2.8}$$

This relationship is identical to the standard Helmholtz resonator equation (Kinsler *et al.* 2000). If the acoustic excitation pressure is zero, then the flow-excited resonance given by (2.4) simplifies to

$$\hat{p}^*_{res} = \hat{F}^*/Z^*, \tag{2.9}$$

where

$$\hat{F}^* = \frac{\int \rho(u\omega_z)^{\wedge}\,\mathrm{d}A}{\frac{1}{2}\rho U^2 L}, \qquad \hat{p}^*_{res} = \frac{\hat{p}_{res}}{\frac{1}{2}\rho U^2}. \tag{2.10}$$

The integrated velocity–vorticity product, denoted here as $\hat{F}^*$, is interpreted to be the dimensionless hydrodynamic forcing that is responsible for exciting the resonator. The magnitude of $\hat{F}^*$ could depend on a number of independent variables, including the geometry of the orifice, the characteristics of the resonator volume and the grazing flow velocity. As such, (2.9) represents the full (nonlinear) momentum balance despite its apparent simplicity. It is of interest to note that the result given by (2.9) is similar to the 'describing function theory' formulation described by Mast & Pierce (1995) and Kook & Mongeau (2002). A derivation is provided in the appendix.

An important assumption that will be employed throughout this paper is that the function $Z^*(f)$ is independent of both the flow velocity and the amplitude of p_{res}. This approximation allows for the direct measurement of $Z^*(f)$, using acoustic excitation (2.8), with subsequent application of the measured function in (2.9). Several results in the literature (e.g. Walker & Charwat 1982; Hersh & Walker 1995) suggest that the grazing flow does not appreciably change the impedance for velocities in the range $U/fL < O(10)$. The assumption that the impedance is not sensitive to the magnitude of the fluctuations has been verified by Ingard & Ising (1967).

Given that direct measurements of the resonator bulk impedance function are available (as described in the following section), (2.9) suggests that the understanding and prediction of flow-excited resonators can be reduced to the study of $\hat{F}^*$. Later it will be shown that the grazing-flow response is essentially harmonic with the peak frequency f_p. This value, represented as $f_p^* = f_p/f_{hr}$, will be a primary dependent variable of interest. The magnitude of $\hat{F}^*(f_p^*)$, as well as of $Z^*(f_p^*)$, determines the magnitude of the unsteady pressure in the resonator. The primary independent variable of interest will be shown to be the dimensionless flow velocity $U^* \equiv U/f_{hr}L$.

3. Resonator acoustic response

The impedance of the resonator, Z^*, was obtained using acoustic excitation. The resonator was placed underneath the empty wind tunnel test section of cross-section 61 cm × 61 cm and a length of 1.83 m. The tunnel inlet consisted of flow-management screens and a contraction located upstream of the test section. Downstream of the test section a diffuser decelerated the air and led to the primary fan. The floor of the test section was the upper wall of the resonator. The resonator had a volume of 0.15 m^3 with a square cross-section of 50 cm × 50 cm and a height of 59 cm. The 12.5 cm × 12.5 cm orifice was cut from a 0.16 cm thick aluminium plate. The edges of the orifice were machined to a 30° angle to form sharp edges. Two 12.5 mm Bruel & Kjaer type 4197 microphones were sampled at a rate of 50 kHz for 84 s.

The resonator impedance was obtained through a two-step process to obtain p_{res}/p_{exc}, where the excitation pressure (p_{exc}) includes only the incident pressure. The measurement was conducted *in situ* in the wind tunnel with no flow. A loudspeaker was placed at the inlet of the wind tunnel with white noise excitation. The first step, shown schematically in figure 3(*a*), used a reference microphone placed in close proximity to the speaker. A second microphone was placed inside the resonator. The frequency-dependent ratio p_{res}/p_{ref} was measured with the orifice opened. In the second step the reference microphone remained at the same location, and the second microphone was located in the wind tunnel test section with the orifice blocked. This measurement provided the ratio p_{exc}/p_{ref}. The function p_{res}/p_{exc}, was obtained by dividing the two transfer functions measured in the first and second steps. This method of determining the resonator impedance was used by Kook (1997).

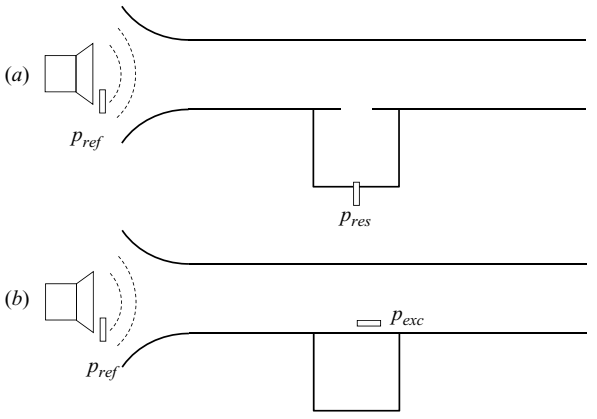

FIGURE 3. Two-step measurement of the resonator response to acoustic excitation: (*a*) step one with orifice open; (*b*) step two with orifice closed.

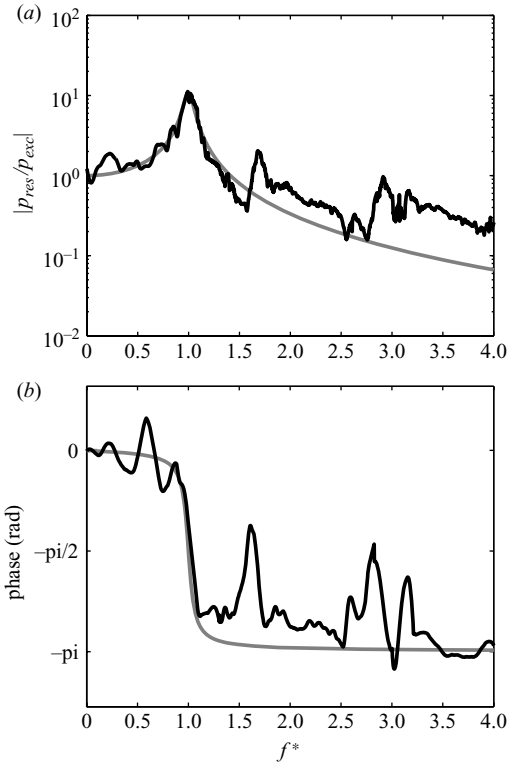

FIGURE 4. (*a*) Amplitude ratio and (*b*) phase angle of resonator acoustic response to acoustic excitation. Grey line denotes the model $1/Z^*_{LEM}$.

The amplitude and phase of the measured resonator response ($1/Z^*$) are shown in figure 4. The Helmholtz resonator frequency f_{hr} was determined to be 46 Hz, and the quality factor Q was found to be 11. The value of f_{hr} is defined as the frequency of the peak of the response, while Q is the magnitude of the response at that frequency. The modelled response $1/Z^*_{LEM}$ is also plotted as a grey line in figure 4 and accurately represents both the amplitude and phase of the impedance at

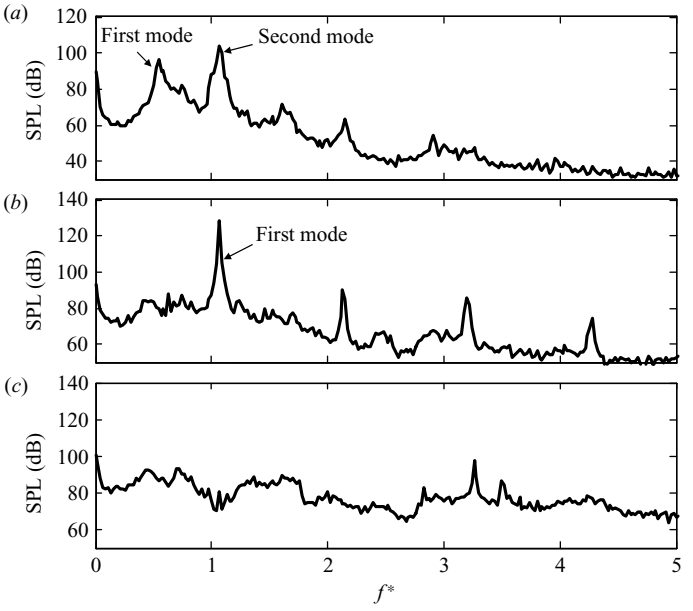

FIGURE 5. Resonator interior sound pressure level at different free stream velocity. (*a*) $U^* = 1.2$; (*b*) $U^* = 2.91$; (*c*) $U^* = 5.31$.

frequencies in the range close to f_{hr}. However, this model was not able to accurately take into account the additional features observed that result from the wind tunnel and surroundings. For example 'peaks' observed near $f^* = 1.7$ and 2.8 are acoustic features of the resonator/wind tunnel system that were not found when the resonator was tested separately. Since the resonator was in the tunnel for the flow-excitation tests, both the measured Z^* and Z^*_{LEM} will be considered in the following sections.

4. Flow-excited resonance

The resonator pressure fluctuations with flow excitation are described in this section. The primary independent variable was the normalized free stream velocity, U^*. The boundary layer profile at the upstream leading edge was measured using a single hot-wire anemometer in order to document the inlet boundary conditions. The boundary layer thickness was found to be 1.65 cm, or $\delta/L = 0.13$. A single microphone was placed inside the resonator. The tunnel velocity was varied from zero to 45 m s^{-1} in increments of 0.28 m s^{-1}, using a computer controlled fan. The microphone was sampled at a frequency of 10 kHz for 13 s at each flow speed. A delay of 10 s was imposed between speed increments in order to allow the tunnel to adjust to the new speed. Measurements were checked for repeatability.

Figure 5 shows the measured sound pressure level (SPL) as a function of f^* at three different flow speeds, $U^* = 1.2$, 2.91 and 5.31. At $U^* = 1.2$, a dual-mode pattern was observed in the spectrum. The first and second modes were observed at $f^* = 0.54$ and $f^* = 1.07$ respectively. At $U^* = 2.91$, the first mode became dominant at $f^* = 1.07$ with a strong peak amplitude of approximately 130 dB. As the flow speed further increased to 5.31, an elevated broadband sound was observed, with no clear sign of resonance.

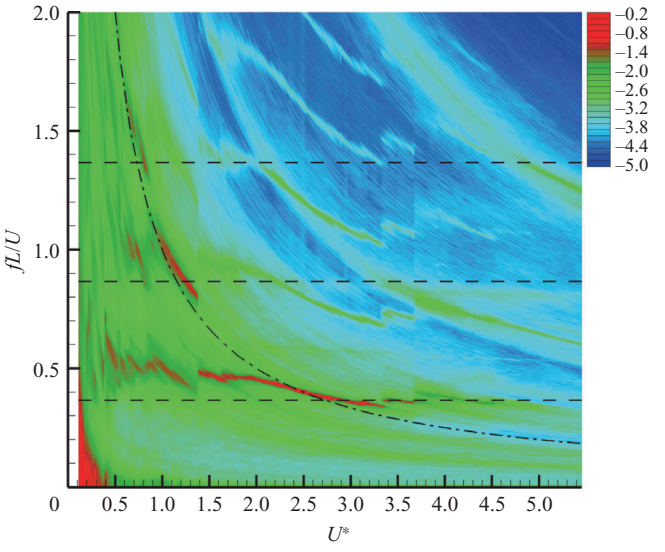

FIGURE 6. Autospectra of the resonator pressure normalized by the free stream dynamic pressure. The dashed–dotted line represents $f = f_{hr}$.

A complete representation of the speed dependence can be obtained by presenting the spectral results as a contour plot as shown in figure 6. The abscissa is U^*; the ordinate represents the frequency normalized as fL/U. The contour variable represents the square root of the spectral values integrated over 1 Hz bins and normalized by the free stream dynamic pressure. The natural hydrodynamic instability frequencies are marked on the figure. These were evaluated from the empirical relationship of Rossiter (1964):

$$\frac{fL}{U} = \frac{n-\alpha}{Ma+1/\kappa}, \quad n = 1, 2, 3, \ldots, \tag{4.1}$$

where Ma is the Mach number; α is a phase delay parameter; and κ is the convection velocity coefficient. The values $\alpha = 0$, $\kappa = 0.38$ were used for the present calculations. The value of α is typically used to adjust the frequency for any phase delay that occurs between the hydrodynamic forcing and the acoustic feedback. In Rossiter's high-speed cavity $\alpha = 0.25$ was found to match the data well. Because the present problem involves the direct interaction of the shear layer with the vertical motion of the resonator orifice, it is argued that there is no phase delay, and thus $\alpha = 0$ is appropriate. The value $\kappa = 0.38$ was based on direct measurements and modelling presented later in this paper. Based on these parameters, the first three modes are predicted to occur at values of $fL/U = 0.37$, 0.87 and 1.37, respectively (shown as horizontal dashed lines in figure 6). Peak resonance of these modes is expected to occur at free stream velocities, where the hydrodynamic instability frequency is close to f_{hr}. The contour representing $f = f_{hr}$ is shown as a dashed–dotted line in figure 6. Large magnitudes are observed in the pressure contours at the expected speed/frequency values.

A number of detailed features can be observed in the spectral contours in addition to the basic resonance phenomenon. The first-mode resonance is observable at low speeds ($U^* < 0.7$). The first, second and third modes can be seen in the range $0.7 < U^* < 1.4$.

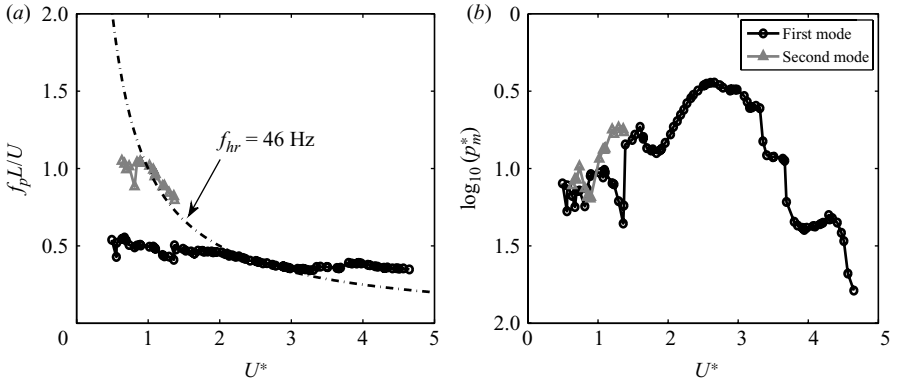

FIGURE 7. Peak frequency and magnitude of p_m^* of the first and second modes.

At higher speeds ($1.4 < U^* < 2.2$) only the first mode is active, and resonance is found to occur at values of fL/U slightly greater than the expected 0.37 value yet lower than $f_{hr}L/U$. As the speed increases further the resonance follows f_{hr} closely, until the peak amplitude point is reached at $fL/U \approx 0.37$, $U^* = 2.72$ as predicted by (4.1). Above this speed the resonance is again observed to occur at a frequency that is between the predicted hydrodynamic frequency and the resonator frequency. The resonance in the range $3 < U^* < 4$ shows a number of 'jumps' in both amplitude and frequency. Similar behaviour can be observed in most of the measurements available in the literature (e.g. Kook & Mongeau 2002; Meissner 2005). In a later section it will be shown that these jumps are a repeatable feature of the flow-excited resonance that is related to the multiple local maxima in the Z^* function noted earlier.

The absolute frequency and magnitude of the resonance shown in figure 6 can be observed more clearly by integrating the spectral densities in the region of the peak resonance as

$$p_m^* = \frac{2}{\rho U^2}\left[\int_{0.8f_p}^{1.2f_p} G_{pp}(f)\,\mathrm{d}f\right]^{1/2}. \tag{4.2}$$

These results are shown in figure 7. The integration limits noted were found to capture the majority of the modal energy without incorporating excess background noise and the like. The values of f_p were found as the maximum in the spectra at each mode as a function of U^*.

An interesting feature of the pressure measurements that is observable in figures 5–7 is the co-existence of both first-mode and second-mode resonance at speeds between $U^* = 1$ and $U^* = 1.4$. The time series of the unsteady resonator pressure was investigated at $U^* = 1.2$ using a wavelet analysis. Specifically, the spectrogram magnitude $WX(f, t)$ is shown in figure 8(a). Two bands centred at 50 Hz (second mode) and 28 Hz (first mode) were observed. In figure 8(b), the wavelet spectral energy was integrated over a narrow bandwidth near the mode-centre frequencies. The contours as well as the integrals show that the two modes do not co-exist at any given time but rather switch back and forth between the two modes. The correlation coefficient between the two time series shown was found to be −0.49. Note that this insight cannot be obtained from the spectral results alone (e.g. figure 5a), since the spectral density is an average that cannot distinguish between two frequencies that exist simultaneously and the intermittent mode switching that was observed here.

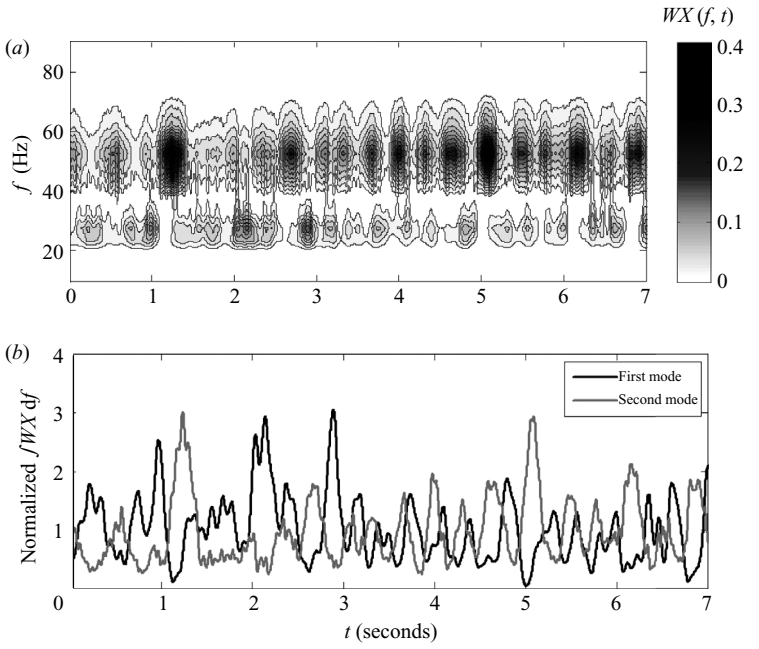

FIGURE 8. (*a*) Contours of Morlet wavelet power spectrum $WX(f,t)$ at $U^* = 1.23$. (*b*) Normalized (by its mean value) integral of $WX(f,t)$ with respect to f for each mode. Black line: first mode ($15 < f < 35$ Hz); grey line: secnd mode ($35 < f < 80$ Hz); correlation coefficient between the two was -0.49.

5. Flow field observations

PIV was used to observe the flow field characteristics in a region near the orifice. A LaVision PIV system with two cameras with resolution of 2048 pixels $\times$ 2048 pixels each were used for the experiments. The cameras were mounted adjacent to each other outside of the wind tunnel and configured for two-component planar measurements. The purpose of using two cameras was to increase the spatial domain without sacrificing resolution. The cameras were angled downwards, such that the field of view extended 3.75 cm into the resonator. A dual-pulsed Nd:YAG laser was mounted on top of the test section. Laser sheet optics were placed on the end of the laser to form the beam into a sheet for PIV imaging. One thousand realizations of the flow were acquired at five flow speeds. The resonator was seeded independent of the free stream before the start of data acquisition.

A microphone was placed in the centre of the floor of the resonator and was sampled simultaneously with the PIV images. The microphone data were sampled at a rate of 33 kHz for 250 ms, starting at 125 ms before the laser was triggered. The laser trigger was also recorded, so that the exact time of the PIV acquisition was known with respect to the microphone time series. A representative time series for the pressure and laser trigger are shown in figure 9.

The resonator pressure signal, as well as the flow field in the vicinity of the orifice, is nearly periodic with a frequency equal to f_p. A useful technique for investigating the flow field is to construct phase-averaged quantities from the PIV measurements. Specifically, a phase value was assigned to each individual PIV realization based on the resonator pressure time series. These phase designations allowed the 1000 realizations obtained at each flow speed to be divided into phase bins. The realizations in each phase bin were then averaged to obtain statistically converged velocity maps of the

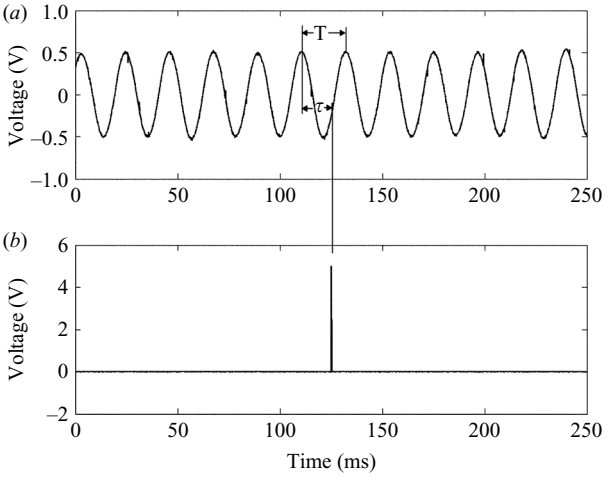

FIGURE 9. Representative time series of raw voltage for (*a*) resonator pressure and (*b*) laser trigger.

flow, with each phase bin having approximately 100 images. The resulting statistics can be considered to be time series of the flow field that have been filtered to pass the mean flow and the resonance frequency harmonics.

The shear layer in the region of the orifice was found to be best observed using the spanwise component of vorticity. These values were computed using a second-order finite difference method applied to the phase-averaged velocity maps. Figure 10 shows contours of $\omega_z L/U$ for three flow speeds, corresponding to $U^* = 1.58$, 2.64 and 3.70 in columns (*b–d*) respectively. Figure 10(*a*) shows the phase of the pressure oscillation for the row of images with the the first row corresponding to the peak pressure; x and y are respectively the streamwise and cross-stream coordinates with their origin located at the upstream edge.

A number of features can be observed in the vorticity field for the three cases shown. The lowest speed ($U^* = 1.58$) corresponds to $p_m^* = 0.18$. The vorticity in the range $0 < x/L < 0.3$ appears to show little unsteadiness in the magnitude of the vorticity, with no observable cross-stream movement of the shear layer. The region $0.3 < x/L < 0.6$ shows significant movement, or 'flapping' of the shear layer, with a corresponding unsteadiness in the vorticity magnitudes. Further downstream ($x/L > 0.6$) the vorticity appears to periodically gather into diffuse regions and 'pinches off' the main shear layer.

The speed $U^* = 2.64$ corresponds to the highest pressure fluctuations in the resonator, $p_m^* = 0.4$. In contrast to the lower speed, the magnitude of the vorticity and the cross-stream location of the shear layer fluctuate significantly in the region $0 < x/L < 0.3$. The three lower phases indicate that the vorticity appears to 'roll up' into a circular, vortex-like structure at the streamwise location $x/L \approx 0.4$. The vortex forms at a cross-stream location that is slightly lower than the plane of the resonator. As this vorticity convects in the streamwise direction it appears to move into the resonator volume. As this occurs the vorticity that remains in the field of view (see the top phase plot in figure 10*c*) forms a relatively thin sheet that extends over the entire orifice.

The highest speed ($U^* = 3.7$) corresponds to $p_m^* = 0.1$. Not surprisingly, the vorticity field indicates significantly less unsteadiness compared to the lower speeds. The vorticity in the region $0 < x/L < 0.4$ shows very little cross-stream movement. The

https://doi.org/10.1017/S0022112008003911 Published online by Cambridge University Press

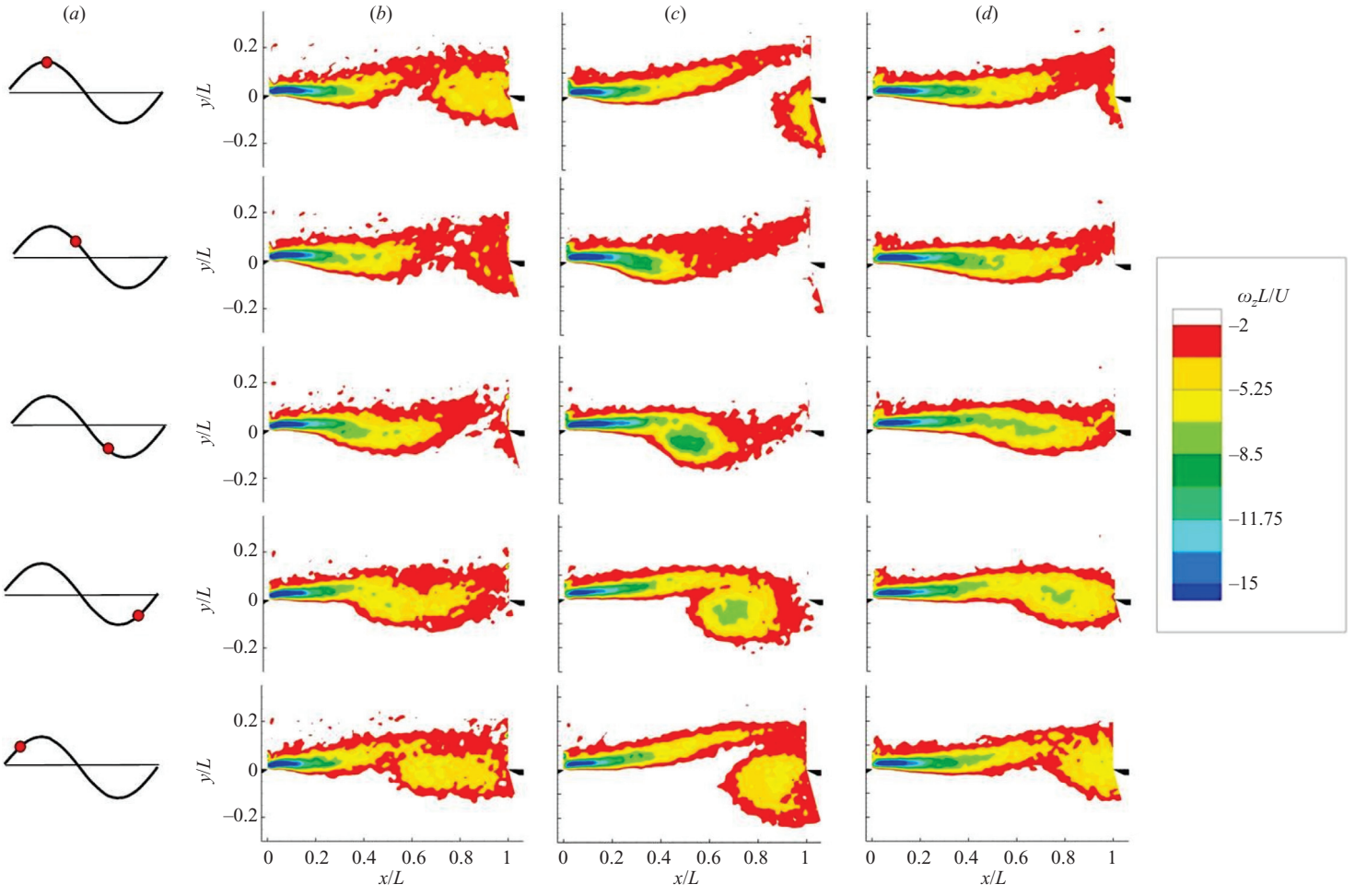

FIGURE 10. Contours of phase averaged vorticity. (*a*) Resonator pressure as a function of phase; dot indicates phase for each row; (*b*) $U^* = 1.58$ (*c*) $U^* = 2.64$; (*d*) $U^* = 3.7$.

vorticity magnitudes fluctuate only slightly in the region $0.4 < x/L < 0.6$, with larger levels of 'flapping' shown to occur only near the downstream edge of the orifice. The structure roughly resembles a discrete vortex in the lowermost phase plot at $x/L \approx 0.7$.

It is of interest to note that most theoretical modelling of the vorticity field considers the flow to be represented either by a perturbed vortex sheet or as a single discrete vortex. The vortex sheet model is used by Elder (1978), Howe (1981) and Chaterllier *et al.* (2004). These models typically ignore the cross-stream distribution of the vorticity by modelling the shear flow as an infinitely thin vortex sheet. The cross-stream location of the sheet is assumed to be periodic in time, with the shape of the sheet dictated by either a prescribed spatial distribution or a set of eigenfunctions. The advantage of this model is that it provides an analytical formulation that can be solved in order to determine the natural instability characteristics of the orifice shear layer. In contrast, the discrete vortex model typically assumes that all of the vorticity in the region of the orifice is rolled up into a single vortex core that convects past the orifice. This type of modelling has been used by Nelson *et al.* (1983), Bruggeman *et al.* (1991), Mast & Pierce (1995), Meissner (2002) and Kook & Mongeau (2002). The advantages of the discrete vortex model are the relative simplicity of the conceptual framework, as well as the ability to model the unsteady forcing. For example Kook & Mongeau (2002) considered the hydrodynamic forcing to be a result of a single vortex passing over the orifice in a given period of the oscillation. The data presented in figure 10 suggests that neither the vortex sheet model nor the discrete vortex model are qualitatively accurate representations of the true vorticity field. Rather, a combination of the two models seems appropriate. Specifically, the upstream region of the orifice resembles a flapping sheet of vorticity in all the speeds shown. The aft region of the orifice appears to show the formation of a single, discrete vortex structure, which partially detaches from the remainder of the vorticity in the region.

A simple view of the time-dependent vorticity magnitude can be obtained by integrating the vorticity values in the cross-stream direction to obtain the circulation density as a function of the streamwise distance and phase angle:

$$\gamma(x, \phi)^* = \int \omega_z^*(x, y, \phi)\, \mathrm{d}(y/L), \tag{5.1}$$

where the values are normalized such that the time average value is given by $\bar{\gamma}^* = 1$. The phase variations in γ^* are shown in figure 11 for the peak resonance speed of $U^* = 2.64$. The five phase values shown are the same as those shown in figure 10. The circulation density plots show a distinct local maximum near the upstream edge of the orifice in the first phase value shown (i.e. maximum resonator pressure). This accumulation of vortical fluid convects at a relatively constant speed across the domain, increases in circulation and grows in size before leaving the field of view at the downstream side of the orifice. As the vortex motion develops and convects across the opening the circulation density at other locations does not fall to zero, as in the point vortex model, but remains at approximately 0.5 throughout the cycle.

A parameter of significant interest in the literature and for the following section is the convection speed of the vorticity. Graf & Durgin (1993) found $U_c = 0.3U$ by looking at the measured vortex position by using LDV. Bruggeman (1987) found values close to $0.4U$ and suggested that the value is due to the boundary layer thickness effects. Kook & Mongeau (2002) used flow visualization and found a value of $0.48U$. Two approaches were used with the present measurements to obtain the net convection speed. First, the speed of the large-scale vortex motion was obtained by tracking the local maximum of the circulation density as shown in figure 11. The speed was calculated as an average over the cycle and normalized by the free stream

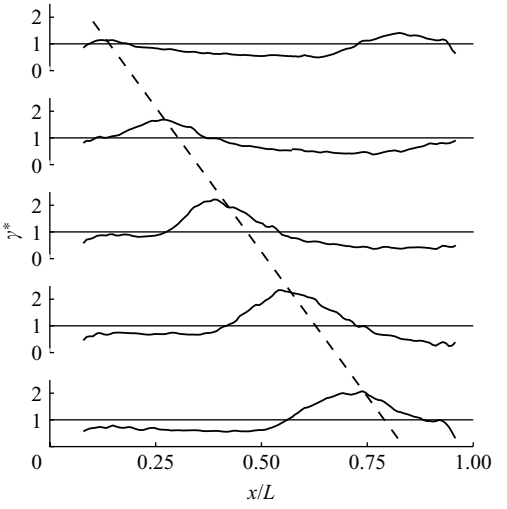

FIGURE 11. Circulation density for five phases (as shown in figure 10*c*) of the flow over one acoustic period.

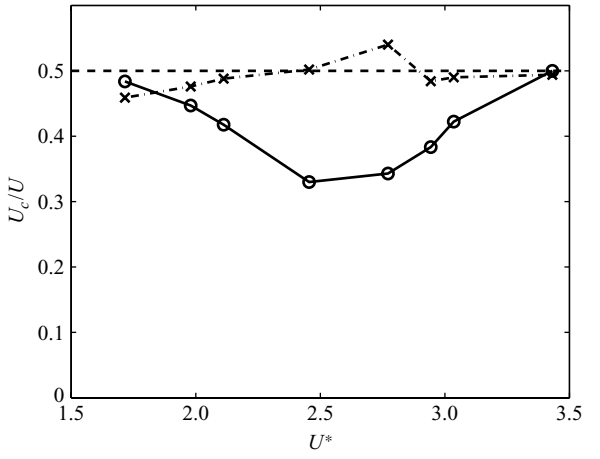

FIGURE 12. Convection speed as a function of U^*: '○' represents U_c from circulation density; '×' represents U_c from (5.2); dashed line represents $U_c = 0.5U$.

velocity. These measurements are shown in figure 12. At lower free stream speeds the vortex velocity is nearly equal to $U/2$. However, closer to the peak resonating speed the vortex motion is considerably slower, with a minimum value observed to be approximately $0.32U$. At higher speeds at which the formation of the discrete vortex is less pronounced the speed was found to be slightly less than $U/2$.

A second method of determining the convection speed can be found from

$$U_c = \frac{1}{\Gamma} \int u\omega_z \, \mathrm{d}A, \tag{5.2}$$

where the circulation and area integral are evaluated over the control volume shown in figure 2. This definition of the convection speed provides a weighted average of the velocity of the vortical fluid over the orifice. These calculations are also shown in figure 12. The measurements indicate that the vorticity as a whole travels very close to the value of $U/2$ regardless of the free stream velocity. This equation takes into

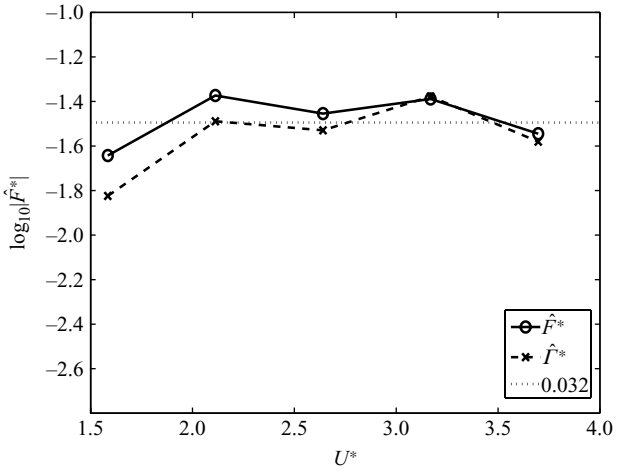

FIGURE 13. Amplitude of $\hat{F}^*$ and the approximation as $\hat{\Gamma}^*$.

account the vorticity in both the 'vortex sheet' and the 'point vortex' regions; so it is thus indicative of the convection speed of the vorticity as a whole, not the convection speed of the vortex alone. Additional commentary regarding the convection velocity will be given in the following section in the context of predicting the resonator pressure fluctuations.

Perhaps the most significant benefit of the PIV measurements is the ability to acquire direct measurements of the hydrodynamic forcing term $\hat{F}^*$ defined in (2.9). The magnitude of $\hat{F}^*$ measured at five flow speeds is shown in figure 13. The data indicate that there is little change in the magnitude of $\hat{F}^*$. In other words, despite the significant ($O(10)$) changes in the resonator pressure with speed – and hence similar changes in the total vertical velocity of the shear layer – the unsteady forcing of the system is relatively constant. The mean value measured was $|\hat{F}^*| = 0.032$. As suggested earlier, this is equivalent to the describing function theory in which the forcing parameter (β in Mast & Pierce 1995 or α/St_ϕ in Kook & Mongeau 2002) is assumed to be a constant.

A simple approximation to the forcing term can be made if the streamwise component of velocity in (2.9) is assumed to be a constant convection speed $U_c = U/2$, such that

$$\hat{F}^* \approx \frac{U_c}{U/2} \int \frac{\hat{\omega}_z}{U/L} \frac{\mathrm{d}A}{L^2} = \frac{U_c}{U/2} \hat{\Gamma}^* = \hat{\Gamma}^*|_{U_c = U/2}. \tag{5.3}$$

This approximation is shown to be reasonable in figure 13, particularly for the higher speeds ($U^* > 2$). The usefulness of this approximation stems from the interpretation that the shear layer forcing can be reduced to the Fourier transform of the circulation contained in the orifice evaluated at the resonating frequency (f_p). This can be further broken down into the unsteady vorticity flux into and out of the orifice region. Specifically,

$$\left(\frac{\mathrm{d}\Gamma}{\mathrm{d}t}\right)^{\wedge}_{in} = \int_{x=0} (u\omega_z)^{\wedge} \,\mathrm{d}y, \qquad \left(\frac{\mathrm{d}\Gamma}{\mathrm{d}t}\right)^{\wedge}_{out} = \int_{x=L} (u\omega_z)^{\wedge} \,\mathrm{d}y \tag{5.4}$$

were evaluated from the PIV measurements, and their non-dimensional results are shown in figure 14. These data show in a more quantitative way how the vorticity is convected into and out of the domain as shown in figure 10. Specifically, the unsteadiness in the rate of influx of circulation is observed to be strongly dependent

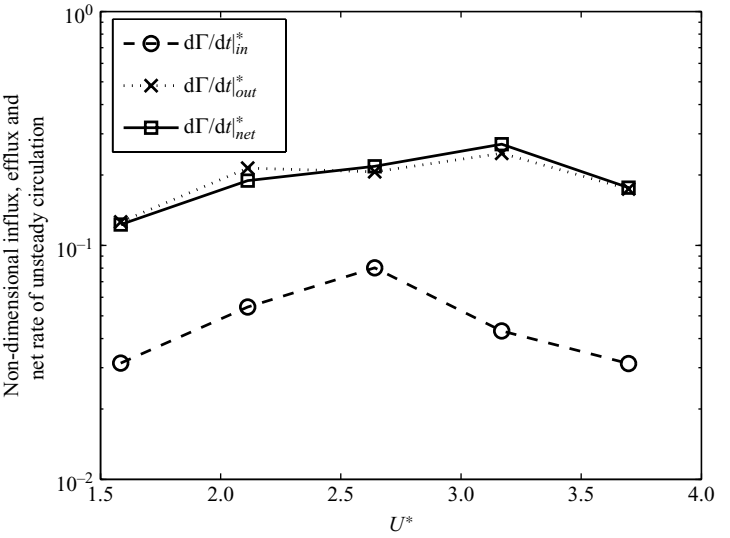

FIGURE 14. Amplitude of the unsteady influx, efflux and net rate of change of circulation.

on speed, with a maximum corresponding to the peak buffeting speed ($U^* \approx 2.7$). Despite these changes, the net unsteady circulation is almost completely determined by the much larger unsteady efflux rate of vorticity.

Independent measurements of the resonator pressure, the impedance function (Z^*) and the forcing function ($\hat{F}^*$) that have been presented allow for an assessment of the assumptions which leads to the simplified expression given in (2.9). First, the amplitude of the resonator pressure fluctuations was estimated from $\hat{F}^*/Z^*_{LEM}(f^*_p)$. These results are presented as open circles along with the directly measured pressure amplitudes (solid line) in figure 15. The comparison is quite good over the speed range. This agreement confirms that the values of $\hat{F}^*$ obtained from the planar PIV measurements are an accurate representation of the true forcing. Second, this result also confirms that the function Z^* measured from the two-step method without the grazing flow provides a very good approximation of the impedance under flow excitation. For reference, figure 15(a) shows the amplitude calculated from the unsteady circulation approximation of the forcing as shown in (5.3). Lastly, the resonator pressure was estimated from (2.5), where $\hat{\xi}$ was evaluated directly from the PIV velocity measurements. These latter approximations provide nominally the same results for the resonator pressure fluctuations as the estimate based on $\hat{F}^*/Z^*_{LEM}(f^*_p)$.

The phase results from the measurements are shown in figure 15(b). The phase of the measured impedance as well as the fitted Z^*_{LEM} are shown as solid curves. By (2.9) the phase difference between $\hat{F}^*$ and $\hat{p}^*_{res}$ should be equal to the phase of Z^*. These data are shown for the directly measured $\hat{F}^*$, as well as for $\hat{\Gamma}^*$. The agreement is quite good, particularly near $f^* = 1$, where the resonator pressure fluctuations are the largest. This agreement provides additional evidence that the derivation of (2.9), the assumption that $Z^*(f)$ can be obtained using a simple acoustic test and the use of the PIV for measuring the forcing function are all reasonable approximations.

6. Prediction of resonator interior pressure

This section presents a method for predicting the resonator pressure fluctuations as functions of the flow speed based on the framework presented. The results will

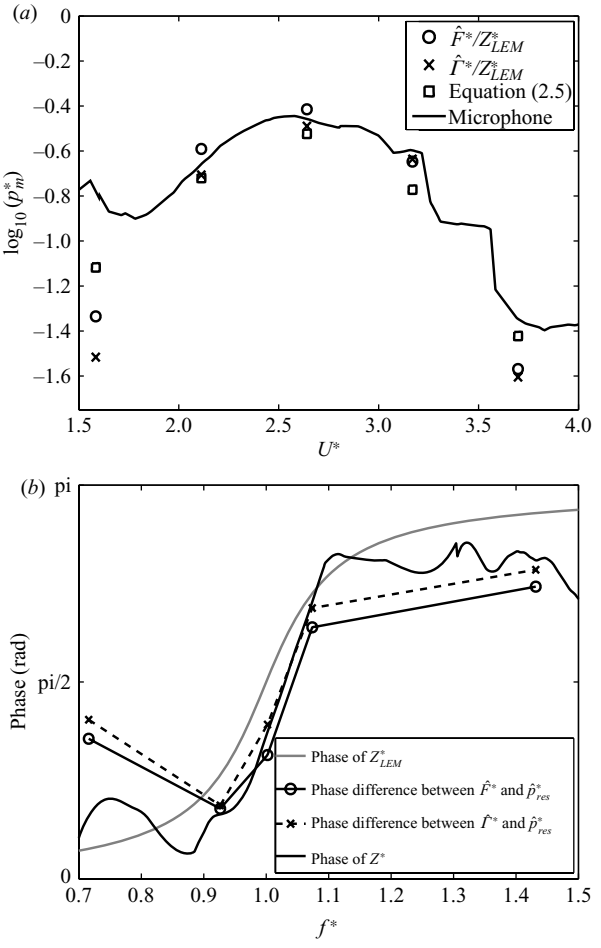

FIGURE 15. Comparison of (*a*) the resonator pressure amplitude with various approximations and (*b*) the phase of Z with the phase difference between the forcing and the resonator pressure.

be compared to the presently acquired measurements, as well as a variety of data available in the literature. The first step of the method involves a model for the determination of the frequency, f_p^*, based on the phase of (2.9). Specifically, the phase difference between the unsteady forcing and the resonator pressure is modelled as $-St_\phi + \pi/2$, where $St_\phi \equiv 2\pi f_p L/U_c$ is a Strouhal number based on the convection velocity. This modelling of the phase delay between $\hat{F}^*$ and $\hat{p}^*_{res}$ was motivated in the described manner: the forcing $\hat{F}^*$ was shown to be equivalent to the unsteady circulation in the region of the orifice, which is almost entirely dominated by the unsteady efflux of vorticity. The vorticity convects across the orifice at a convection speed of U_c, such that a time delay of L/U_c exists between the unsteady circulation and velocity fluctuation $\mathrm{d}\xi/\mathrm{d}t$. In the frequency domain, this time delay is reflected by a phase lag of St_ϕ between the unsteady circulation and $(\mathrm{d}\xi/\mathrm{d}t)\hat{}$. An additional phase difference of $\pi/2$ is added to relate the vertical velocity at the orifice and the resonator pressure, based on (2.5) which was derived for an ideal Helmholtz resonator subjected to harmonic disturbances. Substituting the phase model into (2.9) yields

$$\frac{\hat{F}^*}{\hat{p}^*_{res}} = \frac{|\hat{F}^*|}{|\hat{p}^*_{res}|} \mathrm{e}^{-\mathrm{i}(St_\phi - \pi/2)} = Z^*. \tag{6.1}$$

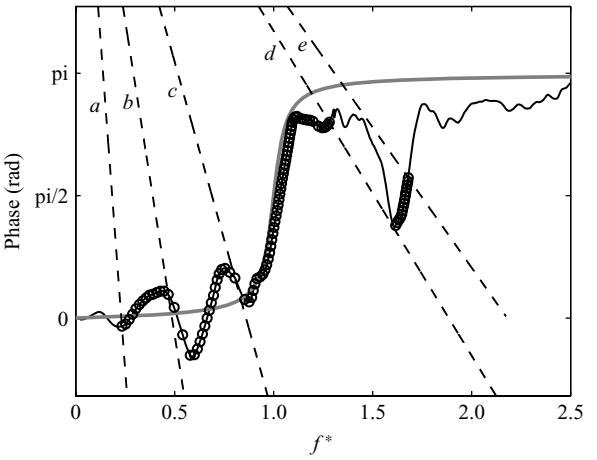

FIGURE 16. Graphical illustration of the f_p solution based on 6.2. Grey curve: phase of Z^*_{LEM}; black curve: phase of measured Z^*; dashed lines (a to e): defined by the left-hand side of (6.2); circle: solution points.

The phase is balanced at discrete frequency values given by

$$-\frac{2\pi f_p L}{U_c} + \frac{\pi}{2} + 2n\pi = phase(Z^*(f_p)), \tag{6.2}$$

where $n = 1$ for the first mode; $n = 2$ for the second mode. Solving (6.2) for f_p is relatively straightforward for U_c and a known function $Z^*(f)$. However, it is of interest to show the solution graphically by plotting the phase values from the two sides of (6.2). This is shown in figure 16, using the phase values from both the measured $Z^*(f^*)$ and Z^*_{LEM}. The straight lines are given for multiple values of U_c for illustration. The intersection of these lines with the $Z^*(f^*)$ function is assumed to give the correct peak frequency, f^*_p. It is of interest to note that the solution to (6.2) will provide a smooth function of f^*_p as a function of U_c when using the fitted function Z^*_{LEM}. In contrast, the solution using the measured Z^* function will have discrete jumps in the f^*_p value as a result of the local maximum that occurs in the true Z^* function. This is shown by the dashed line '*d*' in figure 16. There are also ranges of U_c values (e.g. between lines '*d*' and '*e*') at which there are multiple solutions. In these cases the frequency that corresponds to the minimum value of Z^* was used.

The prediction of the peak frequency as a function of U^* is given in figure 17. A constant ratio of $U_c/U = 0.38$ was used for these calculations. The effects of this ratio on the predictions is discussed below. Note that the ordinate is the frequency scaled by the natural resonator frequency, $f^*_p = f_p/f_{hr}$. The prediction is relatively good over the speed range shown, including both the first and second modes. The discrete jumps in peak frequency that have been observed in earlier discussions are also observed in the predicted values when the true Z^* function is used. Specifically, the resonator constructed was shown to have a secondary local maximum at approximately $f^* = 1.6$ (see figure 4). Both the data and the model indicate that the frequency of the first mode jumps to this secondary frequency value at a velocity slightly higher than that of the peak amplitude. Although the speed of this jump is not predicted well, it is clear from the graphical illustration in figure 16 that spectral smoothing will tend to lower the magnitude of fluctuations in the phase plot and thus will alter the prediction of the speed at which the frequency jumps occur.

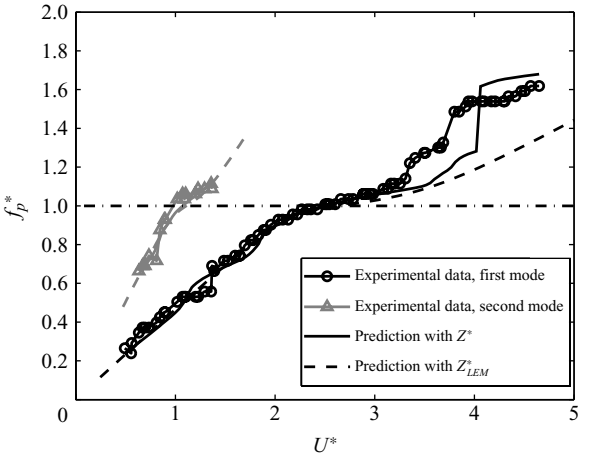

FIGURE 17. Predicted resonance peak frequency and comparison with the experimental data.

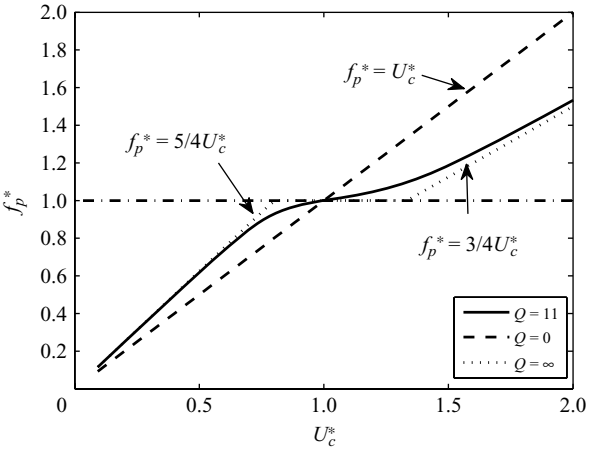

FIGURE 18. Predicted resonance peak frequency as a function of U_c^* at different Q.

It is of interest to use the model given by (6.2) to study the effects of the resonator characteristics on the resonance frequency. For example the peak frequency can be considered as a function of the resonator quality factor Q, using the definition of Z^*_{LEM} given in (2.7). These results are shown in figure 18 for values $Q = 0, 11$ and ∞ as functions of $U_c^* = U_c/f_{hr}L$. The condition $Q = 0$ represents a resonator with infinite damping, such that resonance cannot occur. As expected, the predicted frequency follows a line of $f_pL/U_c = \text{constant}$, illustrating that the shear layer is only subject to the hydrodynamic instability frequency. In the opposite limit, $Q = \infty$ represents the condition of no damping. Interestingly, the theory predicts that the peak frequency follows the line $f_p^* = 5/4U_c^*$ until the condition $f_p^* = 1$ is reached. The resonator is predicted to resonate at the natural frequency for a range of speeds until $U_c^* \approx 1.33$, at which point the frequency increases with a constant slope of 3/4. The value $Q = 11$ represents the resonator described above. The straight line observed for the $Q = \infty$ case is shared by the $Q = 11$ predictions at the lower speeds and well approximated by the data presented in figure 17.

A prediction of the resonator pressure can be made based on the magnitude of the terms in (2.9): $|\hat{p}^*_{res}| = |\hat{F}^*|/|Z^*(f_p)|$. The frequency of resonance f_p is known from

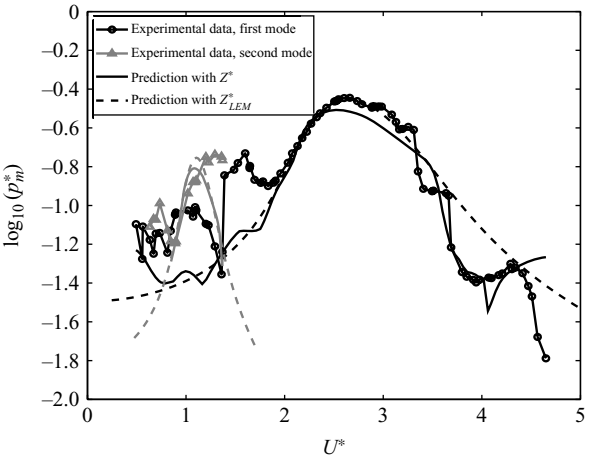

FIGURE 19. Predicted amplitude of the resonator pressure and comparison with the experimental data.

(6.2), and thus $Z^*(f_p)$ is easily calculated for a given flow speed and resonator. The only remaining unknown is the magnitude of the function $|\hat{F}^*|$. The PIV measurements indicate that the values are nearly constant with flow speed, with a mean value of 0.032. The results using this fixed value along with both the measured Z^* and Z^*_{LEM} are shown in figure 19. The predictions match the measured values in the mid-speed range of velocities, where the resonator pressure fluctuations were the largest. At higher velocity the values computed from Z^*_{LEM} are observed to decrease gradually, while the data exhibit sudden 'drops' in amplitude at several speeds. The values computed from the true Z^* function are observed to capture the general character of these features and match the amplitude over most of the speed range. Although these 'jumps' in frequency and corresponding 'drops' in amplitude are not necessarily of primary importance (since they are at speeds higher than the peak resonance) the qualitative and quantitative agreements between the model and the data are thought to provide substantial verification for (6.2) as well as the fact that $|\hat{F}^*|$ can be considered constant.

The ability of the theory to match the frequency and amplitude of the resonator pressure fluctuations that have been described in the literature will now be examined. The comparison of the theory with the present measurements required that the ratio of the net convection speed to the free stream velocity (U_c/U) and the value of $|\hat{F}^*|$ be specified. Rather than assume these parameters to be fixed for all experimental conditions, it will be shown to be of value to allow these quantities to be used as fitting parameters and then subsequently examine how the values depend on the boundary conditions of a given experiment. It was found that matching the theoretical prediction of $f^*_p(U^*)$ to the data required an adjustment of the U_c/U value. From this result, the function $\hat{p}^*_{res}(U^*)$ was matched by adjusting the single constant used for $\hat{F}^*$. The data from Kook & Mongeau (2002), Panton (1990), Elder *et al.* (1982), Meissner (2005), Graf & Durgin (1993) and Nelson *et al.* (1981) were taken from the respective papers. The impedance was modelled as Z^*_{LEM}, based on published values of f_{hr} and Q. A sample of the predictions from the data of Kook & Mongeau (2002), Nelson *et al.* (1981) and Panton (1990) is shown in figure 20. Predictions from the other references noted were similar. These data show very good agreement in terms of both the peak frequency of the resonance and the amplitude.

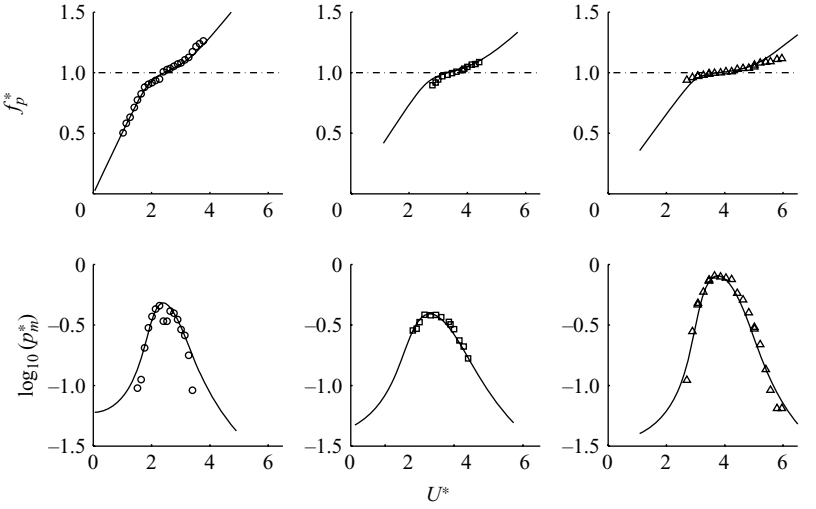

FIGURE 20. Prediction results and comparison with the original experimental data of three cases from literature: circle represents Kook & Mongeau (2002); square represents Nelson *et al.* (1981); triangle represents Panton (1990).

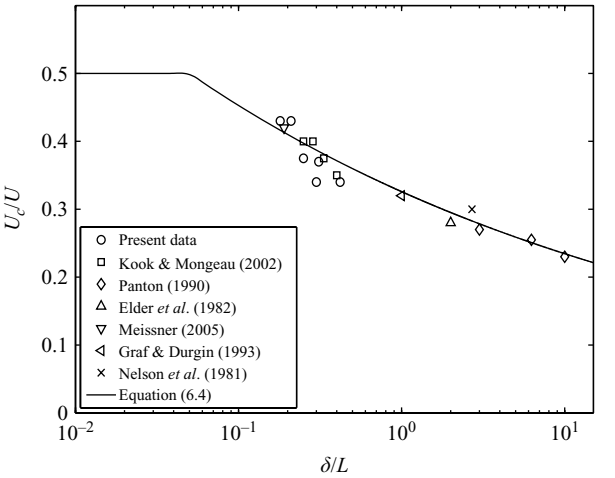

FIGURE 21. Convection velocity data versus δ/L.

The values of U_c/U used to fit the theory to the measured values varied from 0.22 to 0.43. Despite this large variability, a strong correlation was found by plotting U_c/U as a function of δ/L as shown in figure 21. The data show that increasing the boundary layer thickness compared to the length of the window leads to a decrease in the effective convection speed of the vorticity. A physical reasoning for this behaviour can be given in the following manner: consider large δ/L, where only the vorticity in close proximity to the orifice 'participates' in the resonance, and the outer regions of the boundary layer convect far above the opening. This type of inner and outer regions of a shear layer have been described by Morris & Foss (2003). Under these conditions the speed of the vorticity in the inner portion of the boundary layer will convect at a slower speed compared to a thin shear layer in which all of the boundary layer vorticity is involved with the resonance. This reasoning can be used to obtain

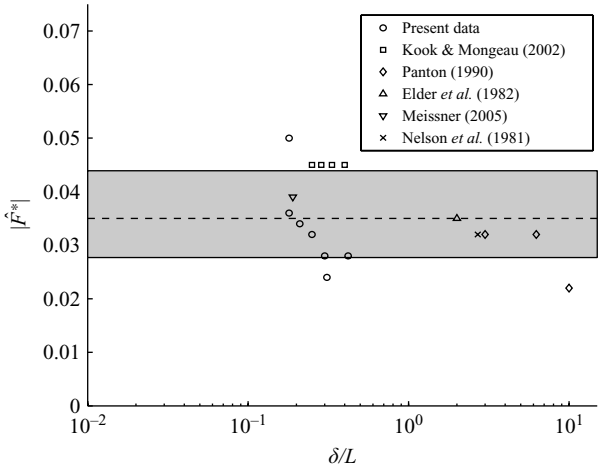

FIGURE 22. Forcing term amplitude data versus δ/L. Dashed line: 0.036; grey region indicating within ± 2 db from the dashed line.

a model for U_c/U as a function of δ/L by assuming that there is a specific location within the boundary layer whose mean velocity can be treated as an 'effective' free stream speed. Specifically, the convection speed can be calculated from

$$\frac{U_c}{U} = \frac{1}{2}\frac{u(y/L = 0.05)}{U} = \frac{1}{2}\left(\frac{0.05}{\delta/L}\right)^{1/7}, \tag{6.3}$$

where the value of $y/L = 0.05$ was chosen to best fit the available data. The final expression in (6.3) was found by replacing the mean velocity profile with a 1/7 power law. The results of this expression are shown as the solid line in figure 21. Note that for small δ/L (where $y/L = 0.05$ is outside the boundary layer), a constant value of 0.5 has been plotted.

As noted, a unique value of $|\hat{F}^*|$ was found for each available data set in order to best match the measured $\hat{p}^*_{res}$. These values were found to vary from 0.025 to 0.05 and are shown in figure 22 as functions of δ/L (for comparison with figure 21). No visible trend was found with δ/L or any other independent variable related to the geometry or acoustic properties of the cavity. A mean value of 0.036, with a standard deviation of 0.008, was found. Although the variability could not be attributed to any specific parameters, using the mean value to predict the resonator pressure fluctuations resulted in a typical error of about 2–3 dB.

7. Conclusions

The analysis and experimental results presented provide a thorough description of the interaction of grazing flow with a Helmholtz resonator. The most significant result of the analysis is the simple relationship given in (2.9): $\hat{p}^*_{res} = \hat{F}^*/Z^*$, as derived from linear momentum. The usefulness of this relationship stems from the interpretation of $\hat{F}^*$ as the hydrodynamic forcing term that is given by the unsteady circulation contained within the domain of the orifice. The application of (2.9) required the potentially restrictive assumption that the collection of terms represented by Z^* could be obtained using acoustic excitation and that the magnitude and phase of Z^* would not change in the presence of the grazing flow. Substantial verification of the assumptions and interpretation was given by providing independent measurements

of $\hat{F}^*$ using the PIV system and comparing the measured values of $\hat{p}^*_{res}$ using a microphone with the calculated values of $\hat{F}^*/Z^*$ as shown in figure 15.

Additional confidence in the theoretical and experimental results was provided by the ability of the model to predict the variations in frequency and magnitude of the resonance that resulted from the multiple features of the true $Z^*(f)$ function. These discrete 'jumps' were typically observed at speeds higher than the peak resonance ($U^* > 2.7$). At lower speeds, however, a different behaviour was discovered in which two distinct shear layer modes would be present intermittently. That is there is a range of flow speeds for which both the first and second shear layer modes were shown to be stable. The result is a random 'mode switching' as shown directly with the time-resolved wavelet analysis.

A significant benefit of the model presented, aside from its predictive capacity, was the ability to gain insight into the effects of the resonator characteristics on the resulting dynamics. Specifically, it was shown that low values of Q lead to resonance at a nearly constant value of fL/U, whereas high values of Q near the peak resonance operate at nearly a fixed value of f/f_{hr}. Similar observations can be made from the data available in the literature.

A number of detailed observations and conclusions have been drawn from the PIV measurements, shown as phase-averaged contours of the spanwise vorticity. Foremost is the observation that the shear layer does not appear as either a flapping vortex sheet or a discrete vortex. The flow does resemble a combination of these two ideals in which the shear layer in the region closer to separation maintains a sheet-like character, and the vorticity in the aft portion of the orifice tends to roll up into a discrete vortex motion that is separated from the vorticity of the incoming boundary layer. Regardless of these dynamics, however, the most important aspect of the shear layer motion is the resulting fluctuations in the net circulation. The PIV data have led to the surprising result that the net unsteady circulation does not vary considerably with flow speed. Moreover, the mean value of 0.032 obtained from the PIV provides an accurate prediction of the resonator pressure at a wide range of flow speeds and is in close agreement with the average value of 0.036 obtained from all of the data available in the literature.

The final point of discussion is the correlation found between the effective convection speed of the vorticity (U_c/U) and the boundary layer thickness (δ/L). The modest scatter among the data presented in figure 21 considering the relatively wide range of resonator types and flow configurations suggests that this is a unique function that is not sensitive to the numerous parameters that are not accounted for (e.g. Reynolds number).

The authors would like to thank Chrysler LLC (Mr. Mark Gleason and Mr. Mitchell Puskarz) for their support of this work.

Appendix. Feedback loop analysis and describing function theory

Feedback loop analysis considers the use of transfer functions to represent the flow excitation and the acoustic response of the resonator in the frequency domain to form a feedback loop. In this loop the flow excitation is regarded as the forward function, and the resonator acoustic response is considered to be the feedback. This requires that the total volume flow rate $\hat{q}$ ($\hat{q} \equiv (\mathrm{d}\xi/\mathrm{d}t)\hat{\wedge}S$) to be split into a 'flow component $\hat{q}_o$ and an 'acoustic component $\hat{q}_r$ as follows:

$$\hat{q} = \hat{q}_o + \hat{q}_r. \tag{A 1}$$

The forward gain function is then expressed as the complex ratio of the flow volume flow $\hat{q}_o$' and the acoustic volume flow $\hat{q}_r$'. The backward gain function is simply the complex ratio of the acoustic volume flow, $\hat{q}_r$, and the flow volume flow, $\hat{q}_o$. The method of using frequency–response functions to represent each of those elements by which a nonlinear system is modelled is called describing function analysis.

Provided that the forward and backward gain functions can be properly modelled, the frequency and amplitude of the limit cycle (stable solution) of the resonator system for a given free stream speed can be obtained by graphically solving the following equation representing the self-consistent condition of the closed feedback loop:

$$\left(\frac{\hat{q}_o}{\hat{q}_r}\right)_f \left(\frac{\hat{q}_r}{\hat{q}_o}\right)_b = 1. \tag{A 2}$$

Different models of the forward and backward gain functions have been proposed in the literature. The most recent work by Mast & Pierce (1995) and Kook & Mongeau (2002) is described here. Since one unknown $\hat{q}$ is split into two unknowns $\hat{q}_o$ and $\hat{q}_r$, following additional equation was introduced by Mast & Pierce (1995):

$$\hat{q}_o = \frac{\hat{p}_{ext} S^2}{i 2\pi f M} = \frac{\hat{p}_{ext}}{Z_M}. \tag{A 3}$$

Here $\hat{p}_{ext}$ denotes the nominal excitation 'pressure due to the grazing flow and is equal to $\hat{F}/L$, and Z_M denotes the acoustic impedance due to the mass M. In this equation, all the acoustic effects including radiation and resonance are neglected, and the resonator opening is considered as a purely mass-like impedance for flow-induced $\hat{p}_{ext}$ and the associated flow volume velocity $\hat{q}_o$. This additional equation basically helps to determine how much $\hat{q}_o$ and $\hat{q}_r$ contribute respectively to the total $\hat{q}$ at different frequencies.

The backward gain function proposed by Mast & Pierce (1995) can be rewritten as

$$\left(\frac{\hat{q}_r}{\hat{q}_o}\right)_b = \frac{Z_M - Z_a}{Z_a}, \tag{A 4}$$

where Z_a denotes the the acoustic impedance of the system, which is equal to $(-4\pi f^2 M + i2\pi f R + K)/(i2\pi f S^2)$. After substituting (A 1) and (A 3) back into it, the backward function (A 3) yields:

$$\frac{\hat{p}_{ext}}{\hat{q}} = Z_a, \tag{A 5}$$

which is the same as (2.9).

REFERENCES

Amandolèse, X., Hèmon, P. & Regardin, C. 2004 An experimental study of the acoustic oscillations by flows over cavities. *J. Vib. Acoust.* **126**, 190–195.

Bruggeman, J. C. 1987 Flow induced pulsations in pipe system. PhD dissertation: Eindhoven University of Technology, Netherlands.

Bruggeman, J. C., Hirschberg, A., van Dongen, M. E. H. & Wijnands, A. P. J. 1991 Self-sustained aero-acoustic pulsations in gas transport systems: experimental study of the influence of closed side branches. *J. Sound Vib.* **150**, 371–393.

Chaterllier, L., Laumonier, J. & Gervais, Y. 2004 Theoretical and experimental investigations of low Mach number turbulent cavity flows. *Exp. Fluids* **36**, 728–740.

Crighton, D. G., Dowling, A. P., Ffowcs Williams, J. E., Heckl, M. & Leppington, F. G. 1992 *Modern Methods in Analytical Acoustics*. Springer.

Crouse, B., Senthooran, S., Freed, D., Balasubramanian, G., Gleason, M., Puskarz, M., Lew, P. & Mongeau, L. 2006 Experimental and numerical investigation of a flow-induced cavity

resonance with application to automobile buffeting. In *12th AIAA/CEAS Aeroacoustics Conf.* Cambridge, MA, USA, 8–10, May 2006.

Dequand, S., Hulshoff, S., van Kuijk, H., Willems, J. & Hirschberg, A. 2003 Helmholtz-like resonator self-sustained oscillations. Part 2: detailed flow measurements and numerical simulations. *AIAA J.* **41**, 416–423.

Dequand, S., Luo, X., Willems, J. & Hirschberg, A. 2003 Helmholtz-like resonator self-sustained oscillations. Part 1: acoustical measurements and analytical models. *AIAA J.* **41**, 408–415.

Dequand, S., Hulshoff, S., van Kuijk, H., Willems, J. & Hirschberg, A. 2003 Helmholtz-like resonator self-sustained oscillations. Part 2: detailed flow measurements and numerical simulations. *AIAA J.* **41**, 416–423.

Dowling, A. P. & Ffowcs Williams, J. E. 1983 *Sound and Sources of Sound*. Halsted.

Elder, S. A. 1978 Self-excited depth-mode resonance for a wall-mounted cavity in turbulent flow. *J. Acoust. Soc. Am.* **64**, 877–890.

Elder, S. A., Farabee, T. M. & DeMetz, F. C. 1982 Mechanisums of flow-excited cavity tones at low Mach number. *J. Acoust. Soc. Am.* **72**, 532–549.

Graf, H. R. & Durgin, W. W. 1993 Measurement of the nonsteady flow field in the opening of a resonating cavity excited by grazing flow. *J. Fluids Struct.* **7**, 387–400.

Hersh, A. S. & Walker, B. E. 1995 Acoustic behavior of Helmholtz resonators: part II. Effects of grazing flow. *CEAS/AIAA* 95-079, 595–604.

Howe, M. S. 1981 The influence of mean shear on unsteady aperture flow, with application to acoustical diffraction and self-sustained cavity oscillations. *J. Fluid Mech.* **109**, 125–146.

Howe, M. S. 1997 Low Strouhal number instabiliies of flow over apertures and wall cavities. *J. Acoust. Soc. Am.* **102**, 772–780.

Inagaki, M., Murata, O., Kondoh, T. & Abe, K. 2002 Numerical prediction of fluid-resonant oscillation at low Mach number. *AIAA J.* **40**, 1823–1829.

Ingard, U. & Ising, H. 1967 Acoustic nonlinearity of an orifice. *J. Acoust. Soc. Am.* **42**, 6–17.

Kinsler, L. E., Frey, A. R., Coppens, A. B. & Sanders, J. V. 2000 *Fundamentals of Acoustics*. Wiley.

Kook, H. 1997 Prediction and control of the interior presure fluctuations in a flow-exciated Helmholtz resonator. PhD dissertation: Purdue University, Lafayette, IN, USA.

Kook, H. & Mongeau, L. 2002 Analysis of the periodic pressure fluctuations induced by flow over a cavity. *J. Sound Vib.* **251**, 823–846.

Mallick, S., Shock, R. & Yakhot, V. 2003 Numerical simulation of the excitation of a Helmholtz resonator by a grazing flow. *J. Acoust. Soc. Am.* **114**, 1833–1840.

Mast, T. D. & Pierce, A. D. 1995 Describing-function theory for flow excited resonators. *J. Acoust. Soc. Am.* **97**, 163–172.

Meissner, M. 2005 The response of a Helmholtz resonator to external excitation. Part II: flow-induced resonance. *Arch. Acoust.* **30**, 57–71.

Morris, S. C. & Foss, J. F. 2003 Turbulent boundary layer to single-stream shear layer: the transition region. *J. Fluid Mech.* **494**, 187–221.

Nelson, P. A., Halliwell, N. A. & Doak, P. E. 1981 Fluid dynamics of a flow excited resonance. Part I: experiment. *J. Sound Vib.* **78**, 15–38.

Nelson, P. A., Halliwell, N. A. & Doak, P. E. 1983 Fluid dynamics of a flow excited resonance. Part II: flow acoustic interaction. *J. Sound Vib.* **91**, 375–402.

Panton, R. L. 1990 Effect of orifice geometry on Helmholtz resonator excitation by grazing flow. *AIAA J.* **28**, 60–65.

Panton, R. L. & Miller, J. M. 1975 Excitation of a Helmholtz resonator by turbulent boundary layer. *J. Acoust. Soc. Am.* **58**, 800–806.

Rockwell, D. & Naudascher, E. 1978 Review-Self-sustaining oscillations of flow past cavities. *J. Fluids Engng* **100**, 152–165.

Rowley, C. W. & Williams, D. R. 2006 Dynamics and control of high-Reynolds-number flow over open cavities. *Annu. Rev. Fluid Mech.* **38**, 251–276.

Rossiter, J. E. 1964 Wind tunnel experiments on the flow over rectangular cavities at subsonic and transonic speeds. *Tech Rep.* 64037. RAE.

Walker, B. E. & Charwat, A. F. 1982 Correlation of the effects of grazing flow on the impedance of Helmholtz resonators. *J. Acoust. Soc. Am.* **72**, 550–555.